IOP Publishing Semiconductor Science and Technology

Semicond. Sci. Technol. **27** (2012) 115011 (6pp) doi:10.1088/0268-1242/27/11/115011

Simulation of fluence-dependent photocurrent in terahertz photoconductive receivers

E Castro-Camus[1], M B Johnston[2] and J Lloyd-Hughes[2]

[1] Centro de Investigaciones en Óptica A C, Loma del Bosque 115, Lomas del Campestre, León, Guanajuato 37150, Mexico
[2] Clarendon Laboratory, Department of Physics, University of Oxford, Parks Road, Oxford OX1 3PU, UK

E-mail: enrique@cio.mx

Received 2 August 2012, in final form 28 August 2012
Published 26 September 2012
Online at stacks.iop.org/SST/27/115011

Abstract

A semi-classical Monte Carlo simulation of carrier dynamics in photoconductive detectors of terahertz (THz) radiation is presented. We have used this simulation to elucidate the importance of carrier trapping in the operation of photoconductive detectors. Simulations of the detection of single-cycle THz pulses by photoconductive antennas based on GaAs with trap densities between 2×10^{17} and 2×10^{18} cm^{-3} are presented. We show that the high frequency (>1 THz) spectral response of photoconductive devices decreases with increasing excitation fluence. Our simulations reveal that this effect is a direct consequence of the saturation of trapping centres

(Some figures may appear in colour only in the online journal)

1. Introduction

Terahertz (THz) time-domain spectroscopy (TDS) has dramatically evolved over the last 25 years [1, 2] to become a relatively well-established technique to access the far-infrared region of the electromagnetic spectrum (between ∼100 GHz and ∼10 THz) [3, 4]. This tool has allowed the study of a large number of systems that range from bulk [5] and nanostructured semiconductors, such as nanowires [6, 7] and quantum wells [8], to proteins [9, 10]. The rapid evolution of this technique is, in part, the consequence of the advances in ultrafast laser technology as well as the progress in understanding of both nonlinear optical processes and carrier dynamics in semiconductors that are used as broadband single-cycle THz emitters [11].

A photoconductive receiver (PCR) detects pulses of THz radiation via the transient photocurrent between metal contacts on a semiconductor surface [12–14]. While PCRs provide a compact and convenient method to detect linear or arbitrarily polarized [15] THz radiation, the photoconductive decay time of the semiconductor material needs to be tailored carefully. The role of the trapping time in the response of PCRs has been discussed previously and two limiting cases were identified [16, 17].

(i) *Direct sampling:* when the decay time of free carriers in the PCR is much shorter than the duration of the THz transient. To a good approximation in this case $E_{\mathrm{THz}}(t_0) \propto I(t_0)$, where $I(t_0)$ is the measured photocurrent as a function of the delay t_0 between the THz and gate pulses.
(ii) *Integrating sampling:* when the lifetime of free carriers in the PCR is much greater than the THz transient's duration. In this case, $E_{\mathrm{THz}}(t_0) \propto \mathrm{d}I(t_0)/\mathrm{d}t_0$ is an appropriate approximation.

In order to improve the signal-to-noise performance of these devices, there is a compromise between carrier lifetime and mobility, which proved to be optimum for lifetimes in between these two regimes. However, care has to be taken to ensure that the photo-excited carrier density is lower than the trap density; otherwise, the carrier density does not decay exponentially. The saturation of traps has been suggested as an explanation for the gate-fluence dependence of the spectral response experimentally observed for THz PCRs [18].

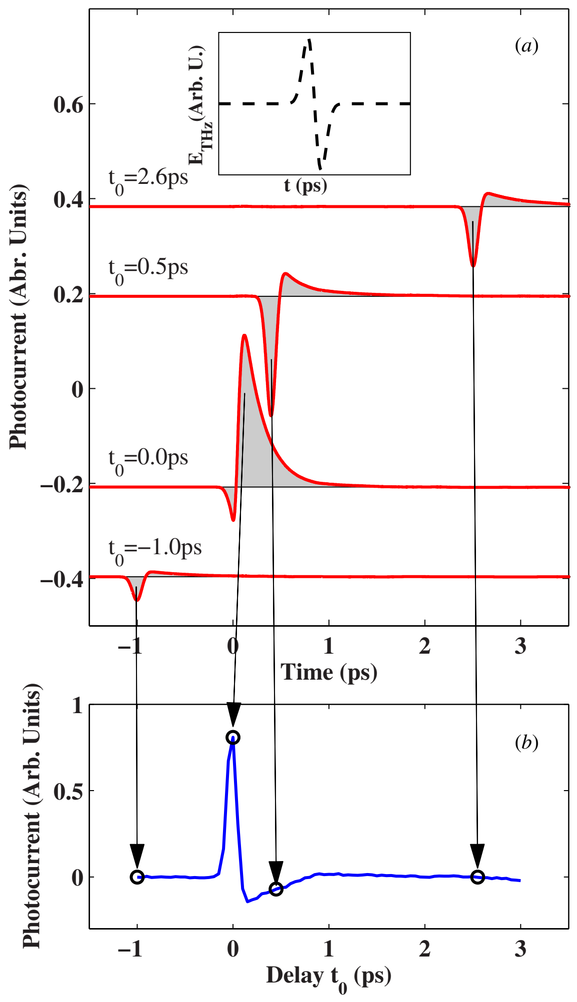

Figure 1. (*a*) The instantaneous photocurrent $I(t, t_0)$ as calculated by the simulation for different delays t_0 between the optical pulse (always arriving at $t = 0$) and the THz pulse. The inset shows the time-dependent THz applied electric field (time scale consistent with main figure). (*b*) The signal measured by a PCR as calculated using equation (3). The circles and arrows denote some of the values that correspond to the specific curves displayed in (*a*) when integrated.

While the dynamics of photocarriers in the surface-field, photo-Dember and photoconductive THz emitters has been well studied [19–29], very little attention has been paid to this aspect for photoconductive detectors. In this paper, we present a semi-classical Monte Carlo simulation of the current response of PCRs to pulsed THz radiation (section 2). The photoconductive material included saturatable traps. The fluence dependence of the THz photocurrent at various trap densities indicates the regimes where a PCR will operate in direct or indirect sampling mode (section 3). Finally, we discuss the carrier–carrier scattering mechanism and its influence on the photocurrent in section 4.

2. Model

2.1. Description

Table 1. Table showing some of the most important parameters for GaAs used in the Monte Carlo simulations presented in this paper.

Parameter	GaAs
Γ valley effective mass	$0.067m_0$
L valley effective mass	$0.56m_0$
X valley effective mass	$0.85m_0$
Hole effective mass	$0.5m_0$
Band-gap energy	1.42 eV
L valley offset	0.29 eV
X valley offset	0.48 eV
β_Γ	1
β_L	4
β_X	3
Def. potential ($\Gamma \rightleftharpoons L$)	0.4 eV Å^{-1}
Def. potential ($\Gamma \rightleftharpoons X$)	2.9 eV Å^{-1}
ϵ_0	12.95
ϵ_∞	10.9
α	1.2×10^6m^{-1}

The three-dimensional semi-classical Monte Carlo model presented here is analogous to one used previously to study THz emitters [19, 20, 30] with two modifications. Firstly, a finite trap density was included resulting in a bi-exponential decay of the number of free carriers, as discussed in section 2.2. Secondly, an externally applied electric field with a temporal profile

$$\mathbf{E}_{\mathrm{THz}}(t) = -\mathbf{E}_0 \frac{t - t_0}{0.4288\,\sigma}\, \mathrm{e}^{-(t-t_0)^2/\sigma^2} \tag{1}$$

was included, where t_0 is the relative delay of the incoming THz pulse, $E_0 = 10$ kV cm^{-1} is its peak amplitude and $\sigma = 0.1$ ps is half of the peak-to-peak time duration (see inset of figure 1(*a*)). This form of $\mathbf{E}_{\mathrm{THz}}$ assumes that the incident radiation field is uniform across the entire simulation volume. This is a good approximation given that the THz field will be diffraction limited, in the best case, and that the THz radiation will take ∼10 fs to go across the photocarrier layer of ∼1 μm.

As low-temperature-grown [31, 32] and ion-implanted [33–36] GaAs are currently the most prevalent materials in PCRs [37], we utilized the parameters of GaAs shown in table 1 (taken from [38] and [39]). The model assumes a thermal distribution of carriers that are present before photoexcitation at a concentration of 2×10^{14} cm^{-3}. The motion of carriers is calculated following Newton's second law

$$\ddot{\mathbf{r}}(\mathbf{r}, t) = \frac{q}{m^*}\,(\mathbf{E}(\mathbf{r}, t))\,, \tag{2}$$

over short periods of time inside a parallelepiped box, where q and m^* are the charge and effective mass of the electron or hole and $\mathbf{E}$ is the total electric field.

At each time step, scattering probabilities are calculated quantum mechanically for the following mechanisms: LO-phonon emission and absorption, TO-phonon intervalley transfer (Γ, L and X) which is proportional to the intervalley deformation potential and the number of final valleys available β_i (with $i = \Gamma$, L and X), acoustic phonon, charged impurity and carrier–carrier scattering [20]. Pseudorandom numbers are used to decide whether each particle is scattered, its scattering angle and energy loss. Subsequently, Poisson's equation is solved over a fine grid across the parallelepiped. The resulting potential is used to calculate the space-charge electric field $\mathbf{E}_\phi$, which when added to the incident THz electric field from equation (1) gives the total electric field **E** acting on each carrier for the next time step.

Carrier photoinjection is performed using a Gaussian temporal and spatial profile (across the surface) with an exponential distribution in the depth direction corresponding to an absorption coefficient α.

In order to model the receiver's response, full sets of simulations were performed for a number of relative delays t_0 between the THz pulse and the gate pulse (always arriving at $t = 0$). The simulated time resolved current $I(t, t_0)$ parallel to $\mathbf{E}_{\mathrm{THz}}$ is shown for various delays t_0 in figure 1(*a*). The photocurrent signal $PC(t_0)$ that would be measured experimentally is assumed to be

$$PC(t_0) \propto \int_{-\infty}^{+\infty} I(t, t_0)\,\mathrm{d}t \tag{3}$$

and is shown in figure 1(*b*). The small current signals seen for $t < 0$ in figure 1(*a*) are the thermal carriers being accelerated by the THz pulse with a relatively fast negative contribution and a smaller long-lived positive tail. The integral of this contribution is substantially smaller (~ 0) than that from the photo-excited carriers (close to $t = 0$).

The data presented in this paper were extracted from 824 individual simulations for different relative THz-gate delays, fluences, trap densities and scattering conditions ran on a 12-core (3.1 GHz) cluster node with 128 GB of RAM. Twelve simulations were run at a time, one on each core, taking ∼48 h of CPU time.

2.2. Trap saturation model

The density of free electrons after photoexcitation is calculated by numerically solving the set of rate equations

$$\frac{\mathrm{d}N}{\mathrm{d}t} = -\frac{N}{\tau_c} - \gamma N(T_0 - T), \tag{4}$$

$$\frac{\mathrm{d}T}{\mathrm{d}t} = \gamma N(T_0 - T), \tag{5}$$

where T_0 is the density of traps, N is the total density of photo-excited electrons, T is the density of occupied traps, τ_c ($\sim$10 ns) [40] is the electron–hole recombination time constant and γ is an electron–trap coupling constant that was set to $\sim 10^{-5}$ cm^3 s^{-1} to fit experimentally available data. The density of photo-excited electrons and the density of occupied traps for various optical fluences (between 2 and 60 μJ cm^{-2}) as function of time are shown in figures 2(*a*) and (*b*), respectively. This calculation was performed assuming a trap density of 2×10^{18} cm^{-3}. The plots show trap saturation within a few femtoseconds for high fluences ($\geqslant$20 μJ cm^{-2}) resulting in slow decay of the photo-excited carrier density. In the case of intermediate fluences ($\sim$6 μJ cm^{-2}) traps become occupied over the first few hundred femtoseconds, resulting in a relatively fast ($\sim$100 fs) reduction of about 70% of the carrier density followed by a slow recombination of the remaining carriers. The low fluence ($\sim$2 μJ cm^{-2}) curve presents a fast quasi-single exponential decay given that only ∼40% of the traps become occupied.

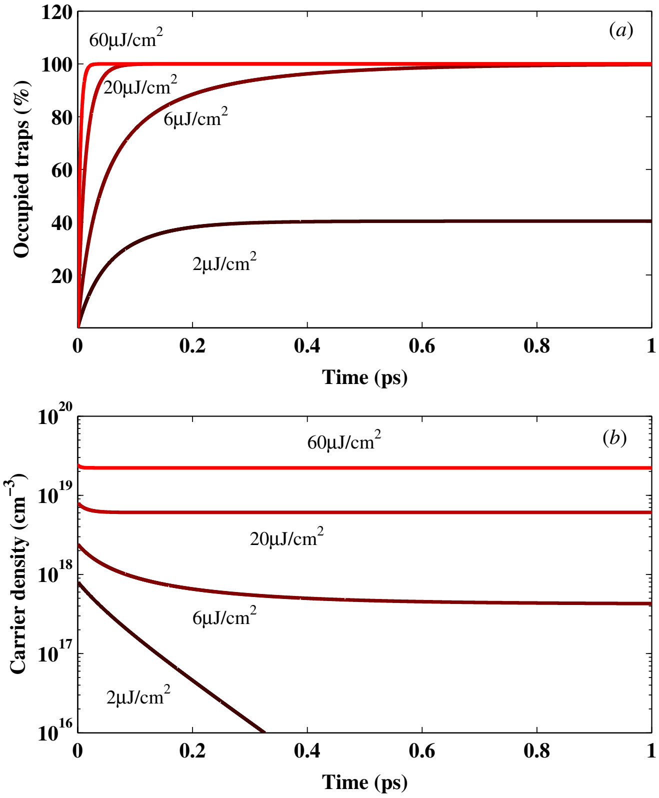

Figure 2. (*a*) Fraction of free charges as a function of time after photoexcitation for optical fluences from 2 μJ cm^{-2} to 60 μJ cm^{-2}. The curves were calculated by numerically solving rate equations (4) and (5). For high fluences it is clear that traps become saturated within the first few femtoseconds, while for the lowest fluence only about 40% of the traps become populated after a picosecond. (*b*) Free carrier density as a function of time for fluences between 2 and 60 μJ cm^{-2}. For lower fluences it is possible to observe quasi-mono exponential, relatively fast trapping of carriers, while at higher fluences the carrier density shows very slow decay. This behaviour is explained by the fast trap saturation shown in (*a*). The calculation was performed assuming a trap density of 2×10^{18} cm^{-3} typical of low-temperature-grown or ion-implanted semiconductors after annealing [17, 41].

3. Influence of fluence

Sets of simulations were performed over a time interval of 3 ps by varying the pump fluence in the range from 2 to 60 μJ cm^{-2}. The resulting integrated photocurrent curves as a function of relative delay are plotted in figures 3(*a*) and (*b*) which correspond to trap densities of 2×10^{17} and 2×10^{18} cm^{-3}, respectively. Note that in figure 3(*b*) the current curves for low fluences are bipolar, showing a direct-sampling-like behaviour. In the case of high fluences, the current curve becomes unipolar which corresponds to an integrating-sampling-like behaviour. This effect is a natural consequence of the trap saturation illustrated in figure 2. The greater degree of trap saturation in the low trap density simulation (figure 3(*a*)) also produces a long-lived current tail after the main pulse which is caused by carriers that follow their ballistic trajectories after the main pulse for a time significantly longer than the pulse duration.

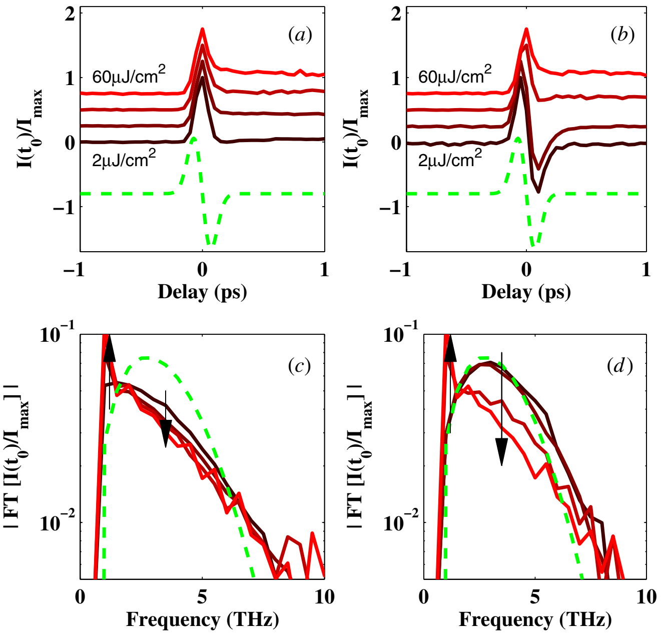

Figure 3. (*a*), (*b*) Normalized current simulated as function of relative delay between optical gate pulse and THz transient for trap densities of 2×10^{17} and 2×10^{18} cm^{-3}, respectively. The dotted line shows the applied THz electric field temporal profile. The curves show the simulations for different gate fluences ranging from 2 to 60 μJ cm^{-2}. The change from bipolar (low fluence) to unipolar (high fluence) shape caused by the trap saturation that increases the effective lifetime of free carriers. (*c*) and (*d*) are the Fourier transform of the curves in (*a*) and (*b*), respectively, the arrows indicate the behaviour of the spectrum at different frequencies as the fluence increases.

The spectral response of photoconductive detectors can be examined by investigating the Fourier transform of the photocurrent, as shown in figures 3(*c*) and (*d*). It is clear that low-frequency components (<1 THz) tend to increase with fluence, due to an enhanced persistent photocurrent. This also produces a modulation in the spectrum caused by the step produced between the first and last points in the time-domain curve.

In the high-frequency region (3.5 THz), the trend is a reduced spectral amplitude with increasing gate fluence. This effect has been observed experimentally before [18]. The spectral effect of the gate fluence is more pronounced in the higher trap density simulations. The 2×10^{17} cm^{-3} trap density simulation becomes saturated even for the lowest gate fluence shown (2 μJ cm^{-2}). In comparison, the simulation with a higher trap density (2×10^{18} cm^{-3}) results in a fast saturation of traps at 60 μJ cm^{-2} and unoccupied traps at 2 μJ cm^{-2}, explaining the difference seen in the simulations.

The PCR's signal amplitude will present a strong dependence on gate fluence. To a first approximation the signal is expected to increase with conductivity, which is proportional to the carrier density and therefore to the gate fluence. Yet, the Monte Carlo model presented here accounts for several other effects, including energy-dependent effective masses or carrier-density-dependent scattering rates for each carrier, in addition to trap saturation, predicting the response of the PCRs more accurately. In figure 4, the simulated signal amplitude for two trap densities is shown at fluences from 0.2 to 200 μJ cm^{-2}. For the low trap density sample, there is a clear sub-linear behaviour (the dotted curve has a gradient of 1), similar to that reported in previous experimental studies [18, 42]. The high trap density simulation has an almost linear dependence for low fluences (<10 μJ cm^{-2}), then a super-linear increase for intermediate fuences (between 10 and 60 μJ cm^{-2}) and a sub-linear dependence for high fluences. The super-linear region is mostly caused by the effective carrier lifetime that increases as traps saturate, therefore producing a super-linear increase of the average conductivity over the duration of the THz pulse.

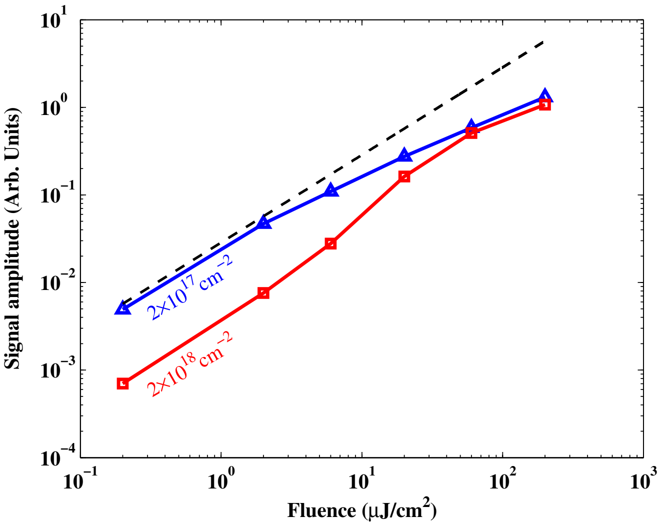

Figure 4. The curves shown are the peak signal amplitudes as a function of gate fluence for trap densities of 2×10^{17} (triangles) and 2×10^{18} cm^{-3} (squares). The dotted line is a linear function provided as a guide to the eye.

4. Influence of scattering mechanisms

Carrier–carrier scattering has been suggested as an additional mechanism that could influence the gate-fluence dependence of photoconductive devices [21]; however, carrier–carrier scattering is an elastic mechanism that might have relatively small effect on the total current. The Monte Carlo model presented here allows this scattering mechanism to be turned on and off, in order to distinguish its contribution to the PCR's response. Simulations at 2 and 60 μJ cm^{-2} with and without including carrier–carrier scattering were performed. The time-domain and Fourier-transformed spectra resulting from these simulations showed no significant change when the carrier–carrier mechanism was excluded as seen in figures 5(*a*) and (*b*). These calculations demonstrate that the effect of carrier–carrier scattering on the receiver's response is negligible compared to the effect of trap saturation.

The evolution of the rates for different scattering mechanisms can be directly extracted from our Monte Carlo simulation. Interestingly, for the simulations where the carrier–carrier scattering is included, it turns out to be the dominant scattering mechanism across most of the simulation. However, for the duration of the THz transient, which is the period when

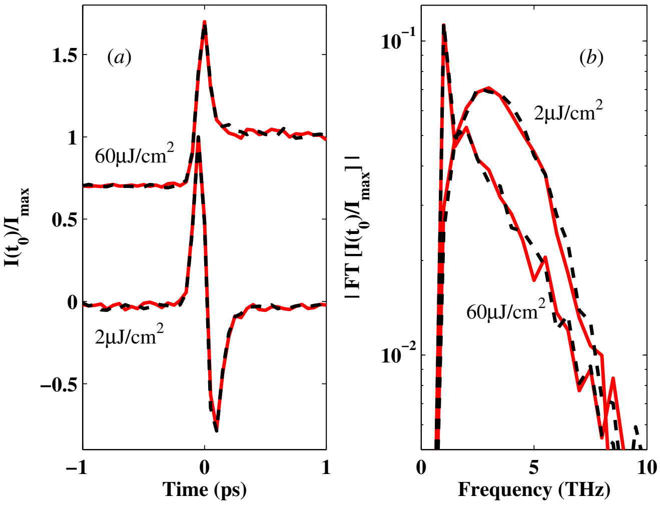

Figure 5. (*a*) Normalized current simulated as a function of relative delay between the optical gate pulse and THz transient. The curves show the simulations for gate fluences 2 and 60 μJ cm^{-2} with (continuous) and without (dashed) carrier–carrier scattering for a GaAs photoconductive detector with a trap density of 2×10^{18} cm^{-3}. (*b*) The Fourier transform of the curves in (*a*). There is a negligible variation between the curves with and without the scattering mechanism.

carriers are strongly accelerated, the carrier–carrier scattering rate becomes comparable to the LO-phonon emission rate $W_{\mathrm{cc}} \approx W_{\mathrm{LO\text{-}em}} \approx 8 \times 10^{12}$ s^{-1} for both the low (2 μJ cm^{-2}) and high (60 μJ cm^{-2}) gate-fluence simulations. Given that LO-phonon scattering is non-elastic, it is expected to produce a greater effect on the current. This explains the negligible effect of carrier–carrier scattering on the photoconductive detector's response.

5. Conclusions

In conclusion, we have presented a Monte Carlo simulation of THz photoconductive detectors and elucidated the role of trap saturation on the time- and frequency-domain response of photoconductive detectors. The contribution of carrier–carrier scattering was found to be marginal in comparison. We expect this simulation to become a very useful tool to design new materials with tailored optoelectronic properties for PCR device applications.

We demonstrated that trap saturation plays an important role in defining the spectral responsivity of PCRs. In order to fabricate photoconductive detectors with either direct sampling or integrating behaviour, this effect has to be taken into account. This has some important implications as follows.

(i) In order to optimize ion-implantation or low-temperature growth and annealing of materials for photoconductive detectors, the gate-fluence regime in which they will be used should be taken into account.
(ii) Different spectroscopic measurements performed with a photoconductive detector should be compared with care when performed at different gate fluences, given that both the responsivity and dynamic range will not be affected evenly across the spectrum.
(iii) The analytic expression for response deconvolution (converting the measured signal to $\mathbf{E}_{\mathrm{THz}}$) presented in [17] is only valid when experiments are performed in the gate-fluence regime below trap saturation.

Auger recombination was not included in this model given that the calculations presented here are for fluences that produce carrier densities well below the regime where this effect is relevant. It might be of interest to include such a mechanism in the future if simulations are to be performed for higher fluences.

Acknowledgments

The authors would like to thank CONACyT (Mexico) (grant no. 131931) and EPSRC (UK) for financial support of this work. We want to acknowledge the use of computational resources from the Supercomputing facility at Centro de Investigaciones en Óptica A C.

References

[1] Tonouchi M 2007 Cutting-edge terahertz technology *Nature Photon.* **1** 97–105
[2] Baxter J B and Guglietta G W 2011 Terahertz spectroscopy *Anal. Chem.* **83** 4342–68
[3] Schmuttenmaer C A 2004 Exploring dynamics in the far-infrared with terahertz spectroscopy *Chem. Rev.* **104** 1759–79
[4] Jepsen P U, Cooke D G and Koch M 2011 Terahertz spectroscopy and imaging—modern techniques and applications *Laser Photon. Rev.* **5** 124–66
[5] Delagnes J C, Mounaix P, Němec H, Fekete L, Kadlec F, Kužel P, Martin M and Mangeney J 2009 High photocarrier mobility in ultrafast ion-irradiated In$_{0.53}$Ga$_{0.47}$As for terahertz applications *J. Phys. D: Appl. Phys.* **42** 195103
[6] Parkinson P, Joyce H J, Gao Q, Tan H H, Zhang X, Zou J, Jagadish C, Herz L M and Johnston M B 2009 Carrier lifetime and mobility enhancement in nearly defect-free core–shell nanowires measured using time-resolved terahertz spectroscopy *Nano Lett.* **9** 3349–53
[7] Baxter J B and Schmuttenmaer C A 2006 Conductivity of ZnO nanowires, nanoparticles, and thin films using time-resolved terahertz spectroscopy *J. Phys. Chem.* B **110** 25229–39
[8] Lloyd-Hughes J, Delley Y L, Scalari G, Fischer M, Liverini V, Beck M and Faist J 2009 Spectroscopic determination of the doping and mobility of terahertz quantum cascade structures *J. Appl. Phys.* **106** 093104
[9] Ebbinghaus S, Kim S J, Heyden M, X Yu, Heugen U, Gruebele M, Leitner D M and Havenith M 2007 An extended dynamical hydration shell around proteins *Proc. Natl Acad. Sci. USA* **104** 20749–52
[10] Castro-Camus E and Johnston M B 2008 Conformational changes of photoactive yellow protein monitored by terahertz spectroscopy *Chem. Phys. Lett.* **455** 289–92
[11] Löffler T, Kreß M, Thomson M, Hahn T, Hasegawa N and Roskos H G 2005 Comparative performance of terahertz emitters in amplifier-laser-based systems *Semicond. Sci. Technol.* **20** S134–41
[12] Tani M, Yamamoto K, Estacio E S, Que C T, Nakajima H, Hibi M, Miyamaru F, Nishizawa S and Hangyo M 2012 Photoconductive emission and detection of terahertz pulsed radiation using semiconductors and semiconductor devices *J. Infrared Millim. Terahertz Waves* **33** 393–404

[13] van Exter M, Fattinger C and Grischkowsky D 1989 High-brightness terahertz beams characterized with an ultrafast detector *Appl. Phys. Lett.* **55** 337

[14] Hatem O, Cunningham J E, Linfield E H, Wood C D, Davies A G, Cannard P J, Robertson M J and Moodie D G 2011 Terahertz-frequency photoconductive detectors fabricated from metal-organic chemical vapor deposition-grown Fe-doped InGaAs *Appl. Phys. Lett.* **98** 121107

[15] Castro-Camus E 2012 Polarization-resolved terahertz time-domain spectroscopy *J. Infrared Millim. Terahertz Waves* **33** 418–30

[16] Tani M, Sakai K and Mimura H 1997 Ultrafast photoconductive detectors based on semi-insulating GaAs and InP *Japan. J. Appl. Phys.* 2 **36** L1175–8

[17] Castro-Camus E, Fu L, Lloyd-Hughes J, Tan H H, Jagadish C and Johnston M B 2008 Photoconductive response correction for detectors of terahertz radiation *J. Appl. Phys.* **104** 053113

[18] Yano R, Gotoh H, Hirayama Y, Miyashita S, Kadoya Y and Hattori T 2005 Terahertz wave detection performance of photoconductive antennas: role of antenna structure and gate pulse intensity *J. Appl. Phys.* **97** 103103

[19] Castro-Camus E, Lloyd-Hughes J and Johnston M B 2005 Three-dimensional carrier-dynamics simulation of terahertz emission from photoconductive switches *Phys. Rev.* B **71** 195301

[20] Johnston M B, Whittaker D M, Corchia A, Davies A G and Linfield E H 2002 Simulation of terahertz generation at semiconductor surfaces *Phys. Rev.* B **65** 165301

[21] Yano R, Gotoh H, Hirayama Y and Miyashita S 2004 Systematic pump-probe terahertz wave emission spectroscopy of a photoconductive antenna fabricated on low-temperature grown GaAs *J. Appl. Phys.* **96** 3635–8

[22] Segschneider G, Jacob F, Löffler T, Roskos H G, Tautz S, Kiesel P and Dohler G 2002 Free-carrier dynamics in low-temperature-grown GaAs at high excitation densities investigated by time-domain terahertz spectroscopy *Phys. Rev.* B **65** 125205

[23] Liu D F and Qin J Y 2003 Carrier dynamics of terahertz emission from low-temperature-grown GaAs *Appl. Opt.* **42** 3678–83

[24] Němec H, Pashkin A, Kužel P, Khazan M, Schnull S and Wilke I 2001 Carrier dynamics in low-temperature grown GaAs studied by terahertz emission spectroscopy *J. Appl. Phys.* **90** 1303–6

[25] Tani M, Matsuura S, Sakai K and Nakashima S 1997 Emission characteristics of photoconductive antennas based on low-temperature-grown GaAs and semi-insulating GaAs *Appl. Opt.* **36** 7853

[26] Cortie D L and Lewis R A 2012 The importance of scattering, surface potential, and vanguard counter-potential in terahertz emission from gallium arsenide *Appl. Phys. Lett.* **100** 261601

[27] Cortie D L and Lewis R A 2011 Role of vanguard counter-potential in terahertz emission due to surface currents explicated by three-dimensional ensemble Monte Carlo simulation *Phys. Rev.* B **84** 155328

[28] Reklaitis A 2010 Terahertz emission from inas induced by photo-Dember effect: hydrodynamic analysis and Monte Carlo simulations *J. Appl. Phys.* **108** 053102

[29] Reklaitis A 2011 Pulsed terahertz emission from GaN/InN heterostructure *J. Appl. Phys.* **110** 103103

[30] Lloyd-Hughes J, Castro-Camus E, Fraser M D, Jagadish C and Johnston M B 2004 Carrier dynamics in ion-implanted GaAs studied by simulation and observation of terahertz emission *Phys. Rev.* B **70** 235330

[31] Gregory I S, Baker C, Tribe W R, Evans M J, Beere H E, Linfield E H, Davies A G and Missous M 2003 High resistivity annealed low-temperature GaAs with 100 fs lifetimes *Appl. Phys. Lett.* **83** 4199–201

[32] Kono S, Tani M, Gu P and Sakai K 2000 Detection of up to 20 THz with a low-temperature-grown GaAs photoconductive antenna gated with 15 fs light pulses *Appl. Phys. Lett.* **77** 4104

[33] Salem B, Morris D, Aimez V, Beerens J, Beauvais J and Houde D 2005 Pulsed photoconductive antenna terahertz sources made on ion-implanted GaAs substrates *J. Phys.: Condes. Matter* **17** 7327

[34] Liu T-A, Tani M, Nakajima M, Hangyo M and Pan C-L 2003 Ultrabroadband terahertz field detection by photoconductive antennas based on multi-energy arsenic-ion-implanted GaAs and semi-insulating GaAs *Appl. Phys. Lett.* **83** 1322–4

[35] Salem B, Morris D, Aimez V, Beauvais J and Houde D 2006 Improved characteristics of a terahertz set-up built with an emitter and a detector made on proton-bombarded GaAs photoconductive materials *Semicond. Sci. Technol.* **21** 283–6

[36] Suzuki M and Tonouchi M 2005 Fe-implanted InGaAs photoconductive terahertz detectors triggered by 1.56 μm femtosecond optical pulses *Appl. Phys. Lett.* **86** 163504

[37] Mangeney J 2012 THz photoconductive antennas made from ion-bombarded semiconductors *J. Infrared Millim. Terahertz Waves* **33** 455–73

[38] Lloyd-Hughes J, Castro-Camus E and Johnston M B 2005 Simulation and optimisation of terahertz emission from InGaAs and InP photoconductive switches *Solid State Commun.* **136** 595–600

[39] Johnston M B, Whittaker D M, Dowd A, Davies A G, Linfield E H, Li X and Ritchie D A 2002 Generation of high-power terahertz pulses in a prism *Opt. Lett.* **27** 1935–7

[40] Lloyd-Hughes J, Merchant S K E, Fu L, Tan H H, Jagadish C, Castro-Camus E and Johnston M B 2006 Influence of surface passivation on ultrafast carrier dynamics and terahertz radiation generation in GaAs *Appl. Phys. Lett.* **89** 232102

[41] Gregory I S, Tey C M, Cullis A G, Evans M J, Beere H E and Farrer I 2006 Two-trap model for carrier lifetime and resistivity behavior in partially annealed GaAs grown at low temperature *Phys. Rev.* B **73** 195201

[42] Winnerl S, Peter F, Nitsche S, Dreyhaupt A, Zimmermann B, Wagner M, Schneider H, Helm M and Kohler K 2008 Generation and detection of THz radiation with scalable antennas based on GaAs substrates with different carrier lifetimes *IEEE J. Sel. Top. Quantum Electron.* **14** 449–57